



Experimental Verification of $n = 0$ Structures for Visible Light

Ernst Jan R. Vesseur,¹ Toon Coenen,¹ Humeyra Caglayan,² Nader Engheta,² and Albert Polman^{1,*}

¹*Center for Nanophotonics, FOM Institute AMOLF, Science Park 104, 1098 XG Amsterdam, Netherlands*

²*Department of Electrical and Systems Engineering, School of Engineering and Applied Science, University of Pennsylvania, 200 South 33rd Street, Philadelphia, Pennsylvania 19104-6314, USA*

(Received 18 May 2012; published 2 January 2013)

We fabricate and characterize a metal-dielectric nanostructure with an effective refractive index $n = 0$ in the visible spectral range. Light is excited in the material at deep subwavelength resolution by a 30-keV electron beam. From the measured spatially and angle-resolved emission patterns, a vanishing phase advance, corresponding to an effective $\epsilon = 0$ and $n = 0$, is directly observed at the cutoff frequency. The wavelength at which this condition is observed can be tuned over the entire visible or near-infrared spectral range by varying the waveguide width. This $n = 0$ plasmonic nanostructure may serve as a new building block in nanoscale optical integrated circuits and to control spontaneous emission as experimentally demonstrated by the strongly enhanced radiative optical density of states over the entire $n = 0$ structure.

DOI: [10.1103/PhysRevLett.110.013902](https://doi.org/10.1103/PhysRevLett.110.013902)

PACS numbers: 42.82.Et, 41.60.-m, 73.20.Mf, 78.66.Sq

In the past several years, developments and advances in the field of electromagnetic metamaterials and plasmonic optics have enabled control over the flow of light in engineered nanomaterials, providing the possibility to realize materials with effective refractive indices that range all the way from positive to negative values [1–5]. These developments have led to exciting features and applications, such as subwavelength imaging and superlensing [6,7], hyperlensing [8–11], cloaking and transformation optics [12–16], and subwavelength scale cavities and waveguides [17,18]. Indeed, the ability to tailor the indices of refraction in engineered nanomaterials has opened many new vistas in the design of optical structures with desired characteristics.

While metamaterials with a negative index have been explored recently, metamaterials and structures with a refractive index near zero have received relatively modest attention (e.g., Refs. [19–23]). Metamaterials with low effective permittivity, i.e., epsilon-near-zero (ENZ) metamaterials, have been studied theoretically [24–34], and some of their characteristics have been investigated experimentally in the microwave frequency [27,28] and mid-IR regimes [35]. Since the index of refraction is directly related to the permittivity via $n = \sqrt{\epsilon\mu}$, these structures exhibit near-zero refractive index. These ENZ metamaterials offer unique and exciting wave characteristics and potential applications such as supercoupling [24–29], displacement-current wires and nanocircuit boards [30,31], antenna-to-waveguide coupling [34], and emission enhancement in plasmonic structures, where the Purcell enhancement may occur almost independently of the location of the emitter [32,33]. There are several approaches to achieve metamaterials and structures with ENZ properties and near-zero refractive index. One way is to design metamaterials by stacking subwavelength

structures such as thin layers [22,23] or embedding complementary metallic split-ring resonators in host media [36]. Another method is by exploiting the dispersion characteristics of composite metal-dielectric waveguides [27,28]—a technique based on structural dispersion instead of material dispersion that has been utilized in the past to construct structures with tailored dispersion characteristics [37]. In particular, it has been shown that a metallic waveguide operating around its cutoff frequency behaves, under proper conditions, as a structure with an effective refractive index and effective permittivity near zero. This concept has been exploited to experimentally verify some of the ENZ properties, such as supercoupling, at microwave frequencies [27,28].

However, to the best of our knowledge, there has been no experimental realization of ENZ metastructures in the visible spectral range nor a demonstration of the exciting characteristics such as enhanced spontaneous emission almost independent of the location of the emitter [33], because fabrication of these structures at optical length scales presents a challenging set of experimental tasks. It is particularly challenging to place an emitter inside an ENZ structure to probe the optical density of states.

In the present work, we show how these challenges can be overcome by bringing together a combination of experimental, theoretical, and numerical efforts. Our ENZ metastructure design is based on a nanoscale dielectric waveguide core surrounded by a metallic cladding (metal-insulator-metal, MIM waveguides) that is designed to operate at the frequency where the waveguide's modal dispersion exhibits cutoff, i.e., $k = 0$. At this frequency, effectively $n = 0$. It is interesting to note that in conventional dielectric waveguides (e.g., waveguides with the core and cladding made of dielectric materials), at the cutoff frequency, the wave number of the mode equals

the propagation constant in the outside medium, and therefore for any frequency below this cutoff, the mode would leak out. Since in such dielectric waveguides, at the cutoff frequency, the wave number is not zero, the phase advance of such a mode is not zero, and thus such a dielectric waveguide at cutoff would not behave as an ENZ or $n = 0$ structure. Here in our geometry we have a MIM rectangular waveguide and therefore near the cutoff frequency the wave number of the mode is small, thus acting similarly to the ENZ and $n = 0$ structures.

We probe the enhanced radiative optical density of states in these ENZ waveguides using a special technique in which we use a 30 keV electron beam as a point dipole source that serves as a spatially resolved probe of the optical density of states.

Figure 1(a) shows a schematic of the waveguide engineered to exhibit $n = 0$ behavior in the visible. The waveguide consists of an 85-nm-thick SiO_2 core that is fully surrounded by a Ag cladding. The structure is fabricated using a sequence of evaporation, sputtering, and focused-ion-beam milling of an SiO_2/Ag layer structure on a Si substrate. Scanning electron micrographs of the fabricated structures are shown in Figs. 1(b) and 1(c).

To probe the dispersion of the waveguide with deep subwavelength accuracy, we utilize a tightly focused (~ 10 nm) electron beam penetrating the waveguide [38,39] from the top as a broadband point dipole emitter [40]. Analogous to a vertical point dipole, coupling of the radiation field of the electron beam to optical modes of the waveguide [41] is governed by the local density of optical states [40,42]. The far-field radiation emitted by the

waveguide, known as cathodoluminescence (CL), is collected in the scanning electron microscope using a parabolic mirror [43] and analyzed using a spectrometer.

Figures 2(a) and 2(b) show a two-dimensional scan of the CL emission over a 400-nm-wide and 2- μm -long waveguide. The recorded intensity is plotted for two wavelengths. The scan clearly shows the outline of the waveguide; it is brighter than the surroundings. The CL emission that is excited along the waveguide shows a strong spatial modulation: at 910 nm emission wavelength we observe 6 maxima along the waveguide axis while at 624 nm 11 maxima are found. We attribute these maxima in CL emission to the antinodes of a standing wave [41,44–46] of the surface plasmon polariton mode that is confined in the 2- μm -long plasmonic Fabry-Perot cavity: the larger number of maxima corresponds to the shorter plasmon wavelength.

The standing wave nodal pattern is plotted for a broad spectral range in Fig. 2(c), which shows a line scan of the CL emission along the waveguide axis; the full emission spectrum is plotted for 5-nm steps along a waveguide with 400-nm width. A large number of resonances is clearly resolved, each corresponding to an integer number of half-wavelengths fitting in the waveguide length. Towards shorter wavelengths, up to 15 antinodes within the waveguide are seen ($\lambda_0 = 500$ nm). The signal vanishes for shorter wavelengths due to increasing losses of the MIM plasmon mode. Figure 2(d) shows a line scan of a 190-nm-wide waveguide. The CL emission for this waveguide shows a completely different behavior. In the 600–700-nm spectral band, this waveguide supports resonances, similar to the wider waveguide, although at a larger period between the maxima. However, at longer wavelengths, the resonances become more closely spaced in the wavelength domain, in contrast to the data for the wider waveguide, where the spacing between the maxima (free spectral range) increases as the wavelength is increased. Correspondingly, for the narrower waveguide, the spacing between maxima along the waveguide rapidly increases with increasing wavelength and at ~ 800 nm the standing wave antinodes merge together in a single band. The constant CL intensity along the MIM waveguide at 800 nm and the fact that no antinodes are observed for longer wavelength clearly show that at this wavelength cutoff occurs. At the cutoff wavelength, the electromagnetic field in the waveguide oscillates in phase along the entire waveguide, corresponding to an effective $n = 0$. Since the mode of this waveguide has a quasi-TE character, the behavior near its cutoff resembles the wave in a structure with an effective zero permittivity or $n = 0$ [32,33]. Therefore, this set of experimental results clearly verifies an ENZ structure at visible wavelength.

For wavelengths longer than the cutoff wavelength, no propagating modes exist and the field of a radiating dipole in the waveguide will decay exponentially. Indeed,

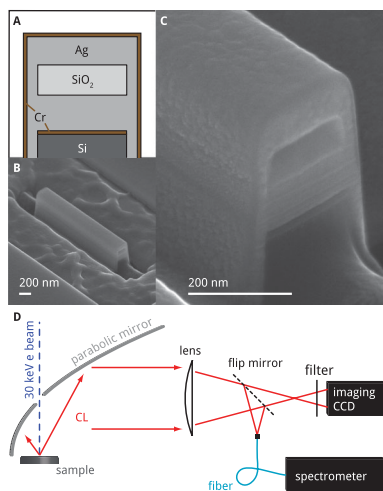


FIG. 1 (color). Experimental structure and measurement setup. (a) Schematic of the end facet of the $n = 0$ waveguide showing the $\text{Si}/\text{Cr}/\text{Ag}/\text{SiO}_2/\text{Ag}/\text{Cr}$ multilayer structure. (b), (c) Scanning electron micrographs of a 2- μm -long, focused-ion-beam fabricated waveguide. (d) Setup for the angle- and spectrally resolved collection of light in the SEM chamber using a parabolic mirror placed over the sample.

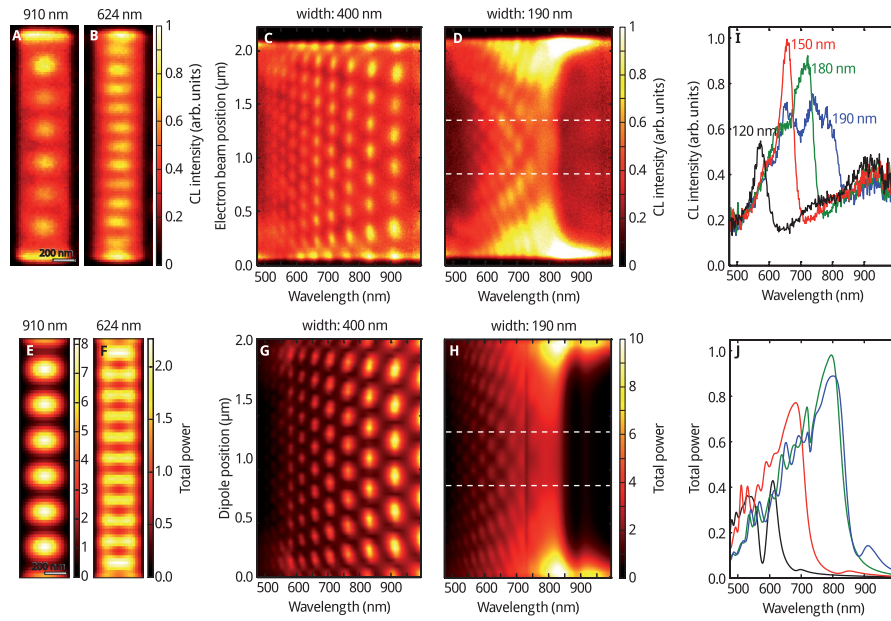


FIG. 2 (color). Subwavelength imaging and spectroscopy of $n > 0$ and $n = 0$ waveguide modes. (a), (b) Experimental results: Excitation maps of the waveguide emission at 910 and 624 nm, respectively, of an 85-nm-thick MIM waveguide with a 400-nm-wide SiO_2 core and a length of $2 \mu\text{m}$, obtained using 30 keV electron-beam excitation. The 2D-scan map in (a) and (b) shows the intensity of the emitted radiation at the indicated wavelength due to the electron beam entering the structure as a function of position of the electron beam (20-nm steps). Clearly, two different resonances are excited, having 7 and 12 half-wavelengths fit in the waveguide length, respectively. (c), (d) Experimental results: Cathodoluminescence spectrum versus electron beam position for MIM waveguides with an 85-nm-thick, 400-nm-wide (c) and 190-nm-wide (d) SiO_2 core. The electron beam was scanned in a line along the axis of the waveguide. The 190-nm-wide waveguide shows cutoff near 800 nm. (e), (f) Simulation results: The total dipole emission intensity from 400-nm-wide and 190-nm-wide waveguides as a function of dipole position. The dipole is positioned within the waveguide core. (g), (h) Simulation results: Dipole emission intensity as a function of position along the waveguide and emission wavelength, analogous to the experimental line scans in (c) and (d). (i) Spectra emitted from MIM waveguides at cutoff (and higher frequencies) with different widths, excited in the region around the center of the waveguide indicated by the dashed lines in (d). Narrower waveguides show cutoff at a wavelength that monotonically decreases with waveguide width. At the cutoff wavelength, the CL emission is strongly enhanced. (j) Simulation results analogous to (i).

Fig. 2(d) shows decaying intensity tails near the ends of the waveguide above 800 nm.

Full-wave numerical simulations utilizing the finite-difference time domain method using the software package LUMERICAL FDTD SOLUTIONS™ [47] were performed using a dipole source placed in the core of the waveguide. Figures 2(e)–2(h) show the simulated total power emitted by the structure, normalized by the power of the dipole emitted in free space. Excellent agreement with the experimental data is obtained, reproducing the standing waves below the cutoff wavelength, a bright band at cutoff, the decaying tails at the waveguide ends, and very low emission above the cutoff wavelength.

To further investigate the relation between cutoff wavelength and waveguide width, Fig. 2(i) shows integrated spectra from a range of waveguides with different widths. Data are taken by integrating spectra over a 500-nm-long line scan along the center of the waveguide. The extent of this region is indicated by the dashed lines in Fig. 2(d). The spectrum for the 190-nm-wide waveguide shows cutoff around 800 nm as evidenced by the sharp decrease in

intensity beyond this wavelength, and a number of resonant peaks at shorter wavelengths, as also observed in Fig. 2(d). For narrower waveguides the cutoff wavelength monotonically shifts towards shorter wavelength: for a 120-nm-wide waveguide cutoff occurs at 570 nm. These data show that cutoff, at which the effective permittivity and effective refractive index is near zero, can be controlled over the full visible or near-infrared spectral range by varying the waveguide width from ~ 100 to 200 nm. In all cases, the emission is clearly enhanced at cutoff [33], an effect that is most pronounced at 150 nm width. These experimental results clearly verify the theoretical predictions for the enhancement of emitter radiation placed inside the plasmonic waveguide at cutoff particularly with the unique property of the uniform phase distribution along the waveguide as described in Ref. [33]. As a consequence, in this structure the Purcell enhancement is independent of the location in the waveguide, in strong contrast with other work in which Purcell enhancement is only observed at specific locations, such as, e.g., enhanced spontaneous emission near an interface [48], modified spontaneous

emission near antennas [49], or in metal nanoparticle arrays [50]. Figure 2(j) presents the simulated analog of Fig. 2(i), showing identical behavior of the enhancement as a function of wavelength and waveguide width. Differences in the peak wavelengths between theory and experiment are attributed to small differences in the geometry and material constants.

From the experimental data, the dispersion of the MIM plasmon mode in this waveguide can be derived (see the Supplemental Material for details [51]). Excellent agreement is obtained with the calculated dispersion over the entire experimental spectral range, including the value of the cutoff wavelength. The dispersion has a small slope towards low frequency corresponding to a strong reduction in the group velocity $v_g = d\omega/dk$, and correspondingly a large increase in density of states. The strongly enhanced CL intensity observed at cutoff is a direct measure of the enhanced density of states. The results are in good agreement with the calculated dispersion in this waveguide, following the theory discussed in Ref. [32].

At cutoff, $k = 0$ and there is no phase advance of the light inside the waveguide; all free electrons of the metallic waveguide oscillate in phase, effectively generating a line dipole. To characterize this special $n = 0$ condition in detail, we measure the angle-resolved CL emission pattern. The radiation, collected by the parabolic mirror, is directed onto a CCD camera; from the image the azimuthal and polar angular distribution of the emission is derived. Figure 3 shows the emission at 700 nm from two waveguides with widths of 210 and 170 nm that are excited by an electron beam at the center of the waveguide. The waveguides are oriented vertically in the figure. At 700 nm, the 210-nm-wide waveguide is far from cutoff and its dispersion lies below the light line. Hence, when this waveguide is excited, the emission at 700 nm mostly emerges from the waveguide ends. Figure 3(a) shows a clear fringe pattern which is attributed to interference of the emission from the two waveguide ends. The narrower 170-nm-wide waveguide is at cutoff at 700 nm. The oscillation in the waveguide is therefore in phase and above the light line, generating a line dipole and thus allowing direct coupling of the plasmon resonance to the far field to the side of the guide (i.e., normal to the line dipole). The measured angular emission pattern at 700 nm in Fig. 3(b) clearly shows two lobes corresponding to the angular emission pattern of a line dipole antenna. This confirms that the waveguide oscillates in phase ($k = 0$). Figures 3(c) and 3(d) show the simulation results using the software package CST MICROWAVE STUDIOTM [52] for the emission patterns, which reproduces both the interference fringes above cutoff and the line dipole emission pattern at cutoff where $n = 0$. The simulations are carried out at 800 nm wavelength, which is the simulated cutoff wavelength for the 170-nm-wide waveguide. Because of slight differences in the cutoff wavelength between the experiment and the

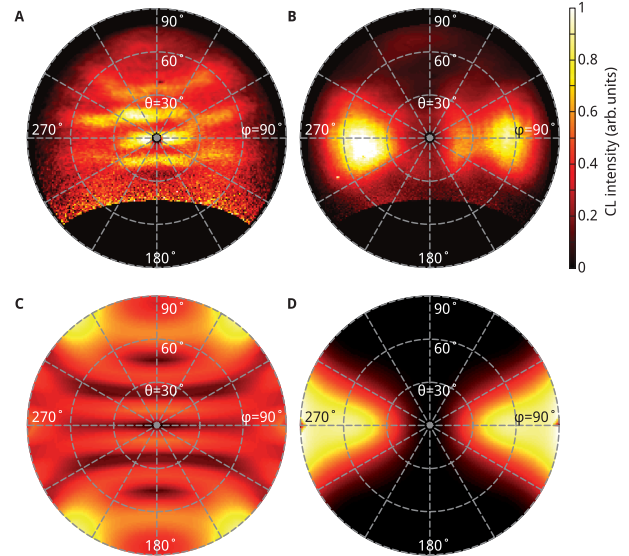


FIG. 3 (color). Angular emission profiles from waveguides above and at cutoff, plotting the azimuthal (φ) and polar (θ) angles. Waveguides are oriented vertically in the figure. (a) A 210-nm-wide waveguide, far from cutoff, shows interference of radiation from the waveguide ends at 700 nm. (b) For the 170-nm-wide waveguide, which is at cutoff at 700 nm, two clear lobes are observed corresponding to radiation from a line dipole (constant phase) along the waveguide. Calculated emission profiles are shown in (c) above cutoff (210-nm-wide waveguide at 800 nm) and (d) at cutoff (170-nm-wide waveguide at 800 nm), which show an upward emission profile that reproduces all features of the experimental data.

simulation as well as slight differences in the end facets, Fig. 3(a) shows the emission of an odd mode whereas Fig. 3(b) shows an even mode [53].

In conclusion, we have fabricated and characterized a nanostructure that guides light with vanishing phase advance ($n = 0$), using a metal-insulator-metal waveguide at cutoff, verifying several important features of the ENZ metamaterials including enhanced emission at cutoff, and uniform phase distribution along the waveguide. Correspondingly, the Purcell enhancement is essentially independent of the location of the emitter placed inside the plasmonic waveguide. Resonant guided plasmon modes buried in the metal-insulator-metal stack were excited using a 30 keV electron beam as a point source exciting the waveguide. Strong modal dispersion is observed, in particular, near the cutoff frequency. The observation of an effective $n = 0$ is corroborated by angle-resolved measurements of the emission that show that the waveguide radiates in a line dipole antenna emission pattern. The metal-insulator-metal plasmon waveguides operating at $n = 0$ provide a key new tool to control dispersion in nanoscale integrated optical circuits and nanolasers and enable enhanced radiative decay rates and superradiance in active metamaterials. By realizing three-dimensional architectures [54] of coupled plasmonic

$n = 0$ waveguides, bulk metamaterials with such properties may be envisioned.

This work is part of the research program “Microscopy and modification of nanostructures with focused electron and ion beams” (MMN) of the “Stichting voor Fundamenteel Onderzoek der Materie” (FOM), which is financially supported by the “Nederlandse organisatie voor Wetenschappelijk Onderzoek” (NWO). The MMN program is cofinanced by FEI Company.

*polman@amolf.nl

- [1] W. Cai and V. Shalaev, *Optical Metamaterials: Fundamentals and Applications* (Springer, New York, 2010).
- [2] J. B. Pendry and D. R. Smith, *Sci. Am.* **295**, 60 (2006).
- [3] S. A. Maier, *Plasmonics: Fundamentals and Applications* (Springer, New York, 2007).
- [4] N. Engheta and R. W. Ziolkowski, *Metamaterials, Physics and Engineering Explorations* (IEEE-Wiley, New York, 2006).
- [5] G. V. Eleftheriades and K. G. Balmain, *Negative-Refraction Metamaterials* (IEEE, New York, 2005).
- [6] J. B. Pendry, *Phys. Rev. Lett.* **85**, 3966 (2000).
- [7] N. Fang, H. Lee, C. Sun, and X. Zhang, *Science* **308**, 534 (2005).
- [8] A. Salandrino and N. Engheta, *Phys. Rev. B* **74**, 075103 (2006).
- [9] Z. Jacob, L. V. Alekseyev, and E. Narimanov, *Opt. Express* **14**, 8247 (2006).
- [10] Z. Liu, H. Lee, Y. Xiong, C. Sun, and X. Zhang, *Science* **315**, 1686 (2007).
- [11] I. I. Smolyaninov, Y.-J. Hung, and C. C. Davis, *Science* **315**, 1699 (2007).
- [12] J. B. Pendry, D. Schurig, and D. R. Smith, *Science* **312**, 1780 (2006).
- [13] D. Schurig, J. J. Mock, B. J. Justice, S. A. Cummer, J. B. Pendry, A. F. Starr, and D. R. Smith, *Science* **314**, 977 (2006).
- [14] U. Leonhardt, *Science* **312**, 1777 (2006).
- [15] A. Alù and N. Engheta, *Phys. Rev. E* **72**, 016623 (2005).
- [16] A. Alù and N. Engheta, *Phys. Rev. Lett.* **102**, 233901 (2009).
- [17] N. Engheta, *IEEE Antennas Wireless Propag. Lett.* **1**, 10 (2002).
- [18] T. Hand, S. Cummer, and N. Engheta, *IEEE Trans. Antennas Propag.* **55**, 1781 (2007).
- [19] R. W. Ziolkowski, *Phys. Rev. E* **70**, 046608 (2004).
- [20] B. T. Schwartz and R. Piestun, *J. Opt. Soc. Am. B* **20**, 2448 (2003).
- [21] S. Enoch, G. Tayeb, P. Sabouroux, N. Guérin, and P. Vincent, *Phys. Rev. Lett.* **89**, 213902 (2002).
- [22] D.-H. Kwon and D. H. Werner, *Opt. Express* **15**, 9267 (2007).
- [23] Z.-H. Jiang, S. Yun, Q. Xu, D. H. Werner, Z. Liu, and T. S. Mayer, in *Proceedings of the IEEE Antennas and Propagation Symposium, Spokane, Washington, 2011* (IEEE, New York, 2011).
- [24] M. G. Silveirinha and N. Engheta, *Phys. Rev. Lett.* **97**, 157403 (2006).
- [25] A. Alù, M. G. Silveirinha, A. Salandrino, and N. Engheta, *Phys. Rev. B* **75**, 155410 (2007).
- [26] M. G. Silveirinha and N. Engheta, *Phys. Rev. B* **76**, 245109 (2007).
- [27] B. Edwards, A. Alù, M. E. Young, M. Silveirinha, and N. Engheta, *Phys. Rev. Lett.* **100**, 033903 (2008).
- [28] B. Edwards, A. Alù, M. G. Silveirinha, and N. Engheta, *J. Appl. Phys.* **105**, 044905 (2009).
- [29] D. A. Powell, A. Alù, B. Edwards, A. Vakil, Y. S. Kivshar, and N. Engheta, *Phys. Rev. B* **79**, 245135 (2009).
- [30] A. Alù and N. Engheta, *Phys. Rev. Lett.* **103**, 143902 (2009).
- [31] N. Engheta, *Phys. World* **23**, 31 (2010).
- [32] A. Alù and N. Engheta, *Phys. Rev. B* **78**, 035440 (2008).
- [33] A. Alù and N. Engheta, *Phys. Rev. Lett.* **103**, 043902 (2009).
- [34] A. Alù and N. Engheta, *IEEE Trans. Antennas Propag.* **58**, 328 (2010).
- [35] D. C. Adams, S. Inampudi, T. Ribaudo, D. Slocum, S. Vangala, N. A. Kuhta, W. D. Goodhue, V. A. Podolskiy, and D. Wasserman, *Phys. Rev. Lett.* **107**, 133901 (2011).
- [36] R. Liu, Q. Cheng, T. Hand, J. J. Mock, T. J. Cui, S. A. Cummer, and D. R. Smith, *Phys. Rev. Lett.* **100**, 023903 (2008).
- [37] W. Rotman, *IRE Trans. Antennas Propag.* **10**, 82 (1962).
- [38] W. Cai, R. Sainidou, J. Xu, A. Polman, and F. J. G. de Abajo, *Nano Lett.* **9**, 1176 (2009).
- [39] M. Kuttge, F. J. G. de Abajo, and A. Polman, *Nano Lett.* **10**, 1537 (2010).
- [40] F. J. G. de Abajo, *Rev. Mod. Phys.* **82**, 209 (2010).
- [41] E. J. R. Vesseur, R. de Waele, M. Kuttge, and A. Polman, *Nano Lett.* **7**, 2843 (2007).
- [42] M. Kuttge, E. J. R. Vesseur, A. F. Koenderink, H. J. Lezec, H. A. Atwater, F. J. Garcia de Abajo, and A. Polman, *Phys. Rev. B* **79**, 113405 (2009).
- [43] T. Coenen, E. J. R. Vesseur, and A. Polman, *Appl. Phys. Lett.* **99**, 143 103 (2011).
- [44] N. Yamamoto, K. Araya, and F. J. G. de Abajo, *Phys. Rev. B* **64**, 205419 (2001).
- [45] N. Yamamoto, M. Nakano, and T. Suzuki, *Surf. Interface Anal.* **38**, 1725 (2006).
- [46] E. J. R. Vesseur, R. de Waele, H. J. Lezec, H. A. Atwater, F. J. G. de Abajo, and A. Polman, *Appl. Phys. Lett.* **92**, 083110 (2008).
- [47] Lumerical FDTD Solutions, Inc., <http://www.lumerical.com>.
- [48] E. Snoeks, A. Lagendijk, and A. Polman, *Phys. Rev. Lett.* **74**, 2459 (1995).
- [49] L. Novotny and N. van Hulst, *Nat. Photonics* **5**, 83 (2011).
- [50] A. F. Koenderink, R. de Waele, J. C. Prangsma, and A. Polman, *Phys. Rev. B* **76**, 201403 (2007).
- [51] See supplemental material at <http://link.aps.org/supplemental/10.1103/PhysRevLett.110.013902> for the dispersion relation.
- [52] CST MICROWAVE STUDIO, <http://www.cst.com>.
- [53] T. Coenen, E. Vesseur, and A. Polman, *ACS Nano* **6**, 1742 (2012).
- [54] S. P. Burgos, R. de Waele, A. Polman, and H. A. Atwater, *Nat. Mater.* **9**, 407 (2010).